remote sensing

MDPI

Article

A Study on the Identification of Geohazards in Henan Province Based on the Basic Deformation Products of LuTan-1

Jing Lu [1], Xinming Tang [1,*], Tao Li [1], Lei Wei [2], Lingfei Guo [2], Xiang Zhang [1] and Xuefei Zhang [1]

[1] Land Satellite Remote Sensing Application Center, Ministry of Natural Resources, Beijing 100048, China; luj@lasac.cn (J.L.); lit@lasac.cn (T.L.); zhangx@lasac.cn (X.Z.); zhangxf@lasac.cn (X.Z.)
[2] Mineral Resources Exploration Center of Henan Geological Bureau, Zhengzhou 450016, China; weilei2507@163.com (L.W.); guolf2025@163.com (L.G.)
* Correspondence: tangxm@lasac.cn; Tel.: +86-139-1188-6268

Highlights

What are the main findings?

- First province-scale geohazard identification using LuTan-1 InSAR products.
- Determining the minimum detectable deformation gradients for DInSAR and SBAS.

What is the implication of the main finding?

- We found 1620 geohazards across Henan Province, proving the applicability of LuTan-1 SAR products in geohazard detection for wide areas.
- SBAS obtained smaller minimum detectable deformation gradients for Henan, proving that it's more usable for deformation monitoring. But DInSAR is better when the coherence is higher than 0.6.

Abstract

Henan Province, characterized by hills and mountains in its western, northern, and southern regions, is a high-risk area for geohazards in China. In this paper, we are the first to investigate the geohazards over Henan using the basic deformation products of LuTan-1, and we provide the minimum detectable deformation gradients of the products. The basic products consist of deformation field products generated by differential interferometric synthetic aperture radar (InSAR, DInSAR) and time-series deformation products derived from multi-temporal InSAR (MT-InSAR). They were produced using the acquisitions from June 2023 to February 2025. We identified 1620 potential geohazards, including 1340 landslides located in western and southern Henan, 139 ground collapses due to underground mining concentrated in the coal-rich central and eastern regions, and 141 cases of ground deformation located mainly in the agricultural areas of central and northern Henan. DInSAR detected 1470 hazards, while MT-InSAR found 150 more. By calculating the deformation between adjacent pixels, we found that the minimum detectable deformation gradients of the 150 geohazards were less than 0.061 mm/m, which is not detectable by DInSAR. The deformation gradients were greater than 0.017 mm/m and were discovered by MT-InSAR. The overall distribution exhibits a certain pattern, offering a basis for geohazard monitoring.

Keywords: LuTan-1; deformation product; Henan province; geohazard; DInSAR; MT-InSAR

check for updates

Academic Editor: Fumio Yamazaki

Received: 28 July 2025
Revised: 29 September 2025
Accepted: 17 October 2025
Published: 23 October 2025

Citation: Lu, J.; Tang, X.; Li, T.; Wei, L.; Guo, L.; Zhang, X.; Zhang, X. A Study on the Identification of Geohazards in Henan Province Based on the Basic Deformation Products of LuTan-1. *Remote Sens.* **2025**, *17*, 3517. https://doi.org/10.3390/rs17213517

Copyright: © 2025 by the authors. Licensee MDPI, Basel, Switzerland. This article is an open access article distributed under the terms and conditions of the Creative Commons Attribution (CC BY) license (https://creativecommons.org/licenses/by/4.0/).

1. Introduction

Henan Province is located in the transitional zone between the North China Plain and the Qinling-Funiu mountain ranges, featuring complex geological structures and widespread loess strata distribution. Coupled with human activities, such as mineral resource extraction and agricultural irrigation, it ranks among China's provinces with the highest frequency of geohazards [1]. Statistics indicate that the hazards in Henan directly threaten over 2 million residents and entail potential economic losses amounting to 12 billion yuan. Influenced by a monsoon climate, the annual average rainfall ranges from 600 to 1200 mm, while extreme rainfall events, like the catastrophic 20 July 2021 Zhengzhou rainstorm, have further heightened risks of rock and soil instability [2]. Henan Province is in the strategic transition of disaster management approach from passive emergency response to proactive prevention and control.

LuTan-1 (LT-1) [3] is China's first satellite dedicated to geohazard monitoring. Its advantages include strong vegetation penetration capability enabled by L-band long-wavelength and 3 m high-resolution imaging mode, combined with a short revisit cycle of 4 days and a full-coverage period of 28 days for China through its pursuit monostatic formation mode. Meanwhile, LT-1 uses dawn–dusk orbit to ensure the sunshine duration time, and the local ascending and descending times are around 18:00 and 6:00, thus the electrons are inactive, and the ionospheric effects are slight. These features allow it to effectively mitigate data decorrelation issues in cloudy and rainy environments, providing a reliable data source for deformation monitoring in complex terrains, such as the loess hilly areas of western Henan Province. To fully leverage LT-1's [4] deformation-monitoring capabilities, we have developed a foundational deformation product system tailored to operational production requirements.

The foundational deformation products consist of deformation field products generated by DInSAR technology and time-series deformation products [5] derived from MT-InSAR technology [6]. Deformation field products are raster datasets created using differential interferometric SAR (DInSAR) technology applied to two co-registered SLC images, generally with a 28-day temporal baseline, where line-of-sight (LOS) deformation measurements directly visualize surface displacement. We use DInSAR data to find the deformation regions. Then, we introduce geology data, archived geohazard databases, meteorological data, and DEM and its slope data, e.g., to separate the geohazards from the deformation regions. By monitoring medium-to-high geohazard-prone zones and adjacent areas, DInSAR detects over 80% of newly emerging geohazards occurring beyond known risk regions. Time-series deformation products are developed through time-series modeling using multiple geometrically calibrated SLC images, presented as scatter plots where each point contains LOS deformation time-series within the interferometric period, and thus, we can assess the stability of the geohazards. To address the complexity and methodological diversity inherent in MT-InSAR systems, the small baseline subset (SBAS) approach is uniformly adopted for on-demand production of these time-series products, ensuring streamlined operational workflows and enhanced compatibility with geohazard-monitoring requirements across diverse terrains.

Based on L-band LT-1 data, this study generated two kinds of basic deformation products for Henan Province using DInSAR and SBAS techniques. Utilizing these deformation results, we interpreted and analyzed the spatial distribution, magnitude, and types of identified geohazards [7]. To validate the InSAR-derived deformation information and investigate the underlying mechanisms of geological hazards in high-risk areas, we conducted a detailed investigation in Lingbao City, a known disaster-prone region in western Henan, employing an integrated interpretation approach. Subsequently, based on the

validation results from this comprehensive investigation, we discuss the capabilities of the DInSAR method in detecting surface deformation associated with geological hazards.

Section 2 introduces the geohazard background of the study area and describes the datasets used for both methods. Section 3 presents the processing methodologies for DInSAR and SBAS techniques, including an analysis of their minimum detectable deformation velocity gradients. Section 4 details the InSAR-derived results, provides their interpretation, and further discusses the minimum detectable deformation gradients for both DInSAR and SBAS methods. Finally, Section 5 summarizes the key findings and conclusions.

2. Materials and Methods

2.1. Study Area

Henan Province, with 44.3% of its land being mountainous and hilly, is highly vulnerable, particularly in its western, northern, and southern highlands, as well as the northern plains and eastern areas. Geohazards in Henan have increased, especially before the flood season from June to September, and now occur year-round due to climate change and human activities. Heavy rainfall and snow-melt significantly raise the risk of debris flows and landslides.

Geohazards in Henan province predominantly occur in known hazard-prone areas and concentrate during the flood season, primarily triggered by heavy rainfall [2]. Furthermore, human activities also serve as a contributing factor. These hazards mainly manifest as collapses, landslides [8], and human-induced ground deformation [9]. From 2011 to 2022, Henan Province experienced nearly 812 geohazards, resulting in 11 deaths [10]. Currently, there are thousands of known geohazards in Henan Province, threatening 165,200 people and property valued at 6.611 billion yuan. Based on the stage of gully evolution, the geohazard susceptibility of Henan Province was zoned into four regions. Areas of extremely high susceptibility to geohazards are predominantly located in the mountainous and hilly regions of northern Henan's Taihang Mountains, western Henan's Xiaoshan, Xiong'ershan, Funiu Mountains, Songshan, and Wai Fangshan, as well as southern Henan's Tongbai Mountains and Dabie Mountains. A total of 1080 small watersheds were delineated, covering a total area of 33,074.51 square kilometers [11].

Lingbao City, a representative geohazard hot spot in western Henan Province, is located at the southeastern edge of the Loess Plateau. It is bordered by the Xiaoqinling-Xiaoshan Mountains to the south and the Yellow River valley to the north. The significant geohazards in this region result from the interplay of three critical factors: thick, erosion-prone loess deposits, ongoing tectonic uplift along the Qinling orogenic belt, and extensive landform changes induced by mining. This natural–human synergy makes Lingbao an ideal model for investigating hazard dynamics within provincial-scale disaster corridors.

2.2. Datasets

Firstly, we utilized 2800 LT-1 acquisitions with 3 m resolution acquired from July 2023 to Dec. 2024 across Henan Province, encompassing 1428 ascending-orbit and 1372 descending-orbit acquisitions (Table 1), along with the 30 m resolution TanDEM-DEM as external DEM data, to perform DInSAR processing. The descending-orbit acquisitions and interferograms using DInSAR are shown in Figure 1.

Table 1. Main parameters of LT-1 and data usage of the two methods.

Parameter	DInSAR		SBAS	
Band	L			
Wavelength (cm)	23.8 cm			
Azimuth/Range pixel spacing	1.74 m/1.67 m			
Azimuth/Ground range look	4:2			
Polarization	HH			
Acquisition time	June 2023–December 2024		July 2023–February 2025	
Orbit direction	Ascending	Descending	Ascending	Descending
Number of acquisitions	1428	1372	540	1176

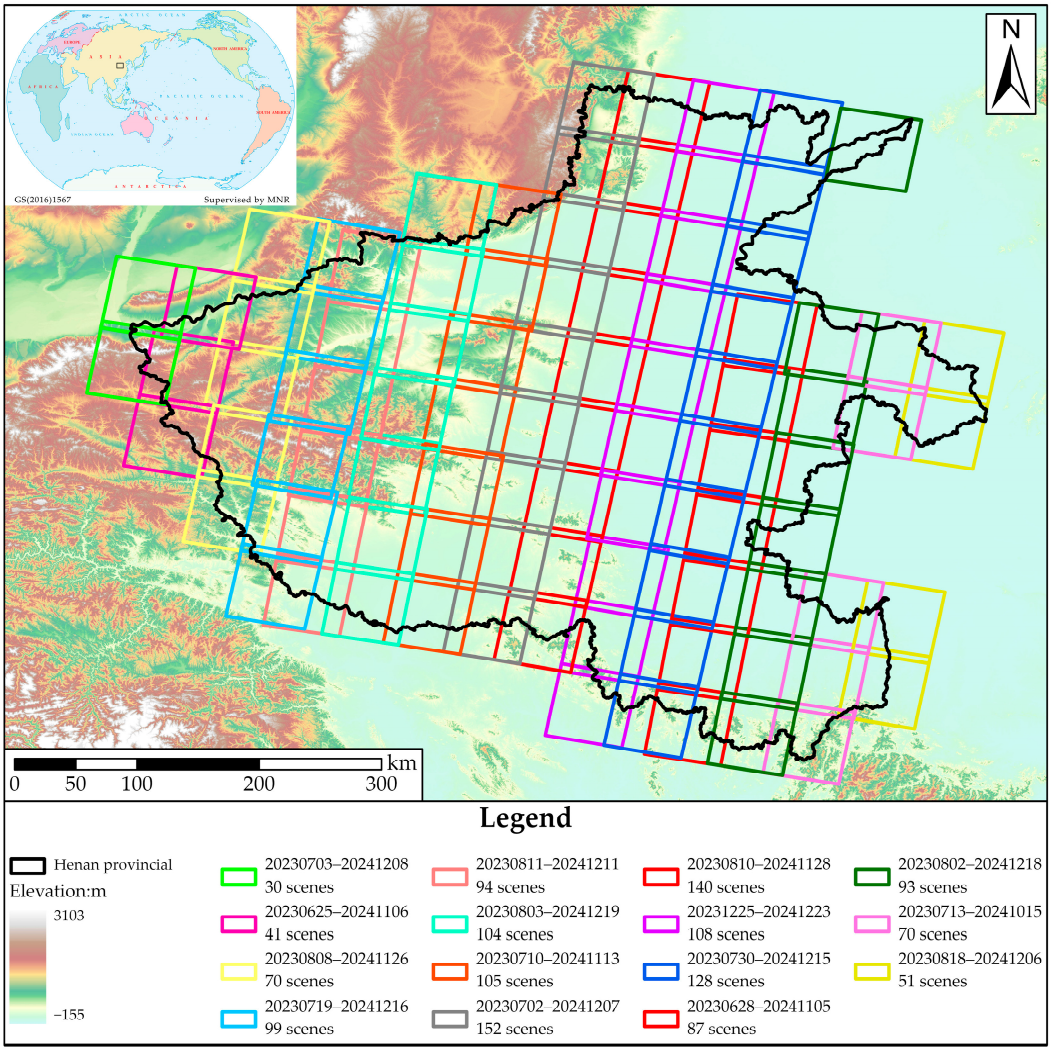


Figure 1. The descending-orbit acquisitions and interferograms using DInSAR.

Secondly, we removed some images that had erratic frames in order to ensure processing efficiency. There were 1716 images selected to conduct the SBAS analysis. The acquisitions, with a 3 m spatial resolution, included 540 ascending-orbit and 1176 descending-orbit data acquired from July 2023 to February 2025. These small baseline interferograms were subsequently inverted to derive mean deformation rate fields. Furthermore, we integrated mining area boundaries into our deformation-screening method, and we overlaid optical imagery and topographic data to facilitate a three-dimensional interpretation. This approach allowed us to preliminarily identify geological hazards and gather basic information about the elements at risk during the screening process.

Thirdly, during the deformation interpretation process, we conducted a detailed investigation and field survey in Lingbao City.

2.3. Production Methods and Minimum Detectable Deformation Velocity Gradients

In this study, DInSAR and SBAS [12] processing were performed using LandSAR software 1.5.0 version [13], which was developed by our team. Interferograms were generated using the constraints of 1500 m for perpendicular baseline and 150 days for temporal baselines, importing the precise orbit data to remove the orbit error. The flattening and topographic effects were removed with the TanDEM-DEM. Then, adaptive filtering and phase unwrapping were used to obtain a series of unwrapped differential interferograms. The influence of decorrelation/thermal noise phase can be weakened by filtering. Because the study area is located in a mountainous area, a simple linear model was employed to remove the topography-dependent atmospheric phase:

$$\phi_{\text{int}} = \phi_{def} + \phi_{flat} + \phi_{atm} + \phi_{orb} + \phi_{topo} + \phi_{noise} \tag{1}$$

In this formula, ϕ_{def}, ϕ_{flat}, ϕ_{atm}, ϕ_{orb}, ϕ_{topo}, and ϕ_{noise} represent deformation phase, flat phase, atmospheric phase, orbit error phase, terrain phase, and noise phase, respectively. We calculate the deformation phase by removing all other components. That also means DInSAR is affected by those four components, and the data are not as robust as the SBAS. We need to remove all the systematic errors, such as the flat phase, orbital phase, and topographic phase [14], and the Generic Atmospheric Correction Online Service for InSAR (GACOS) [15] is used to remove the atmospheric phase. Finally, the coherence value is used to assess the minimum detectable deformation gradient [16,17]:

$$\Delta\phi^{\min}_{(\gamma,N)} = (0.000003696 \times \mu(N) - 0.0002473) \times (\gamma - 1) + 0.0000007 \tag{2}$$

where μ is the resolution, N is the multi-looking factor, and λ is the coherence.

The SBAS [18] technique uses all the interferograms that satisfy the conditions of temporal–spatial baseline thresholds, see Figure 2. When analyzing the capability of the SBAS [19], we need to use the relative phase observation along arcs connecting the persistent scatterer (PS):

$$\Delta\varphi^{k}_{(x,y)} = -\frac{4\pi}{\lambda}\Delta v_{(x,y)}T^{k} - \frac{4\pi B^{k}_{\perp}}{\lambda R\sin\theta}\Delta\varepsilon_{(x,y)} + \omega^{k}_{(x,y)} \tag{3}$$

Then, we convert the phase gradient along arcs into the relative deformation rate by using the following:

$$\Delta v_{(x,y)} = -\frac{\lambda}{4\pi T^{k}}\Delta\varphi^{k}_{(x,y)} - \frac{B^{k}_{\perp}}{R\sin\theta T^{k}}\Delta\varepsilon_{(x,y)} + \frac{\lambda}{4\pi T^{k}}\omega^{k}_{(x,y)} \tag{4}$$

where ω is the phase residues along arcs; it is expressed by using the following:

$$\omega^{k}_{(x,y)} = \sqrt{-2\ln|\gamma_{t}|} \tag{5}$$

where γ_t is the temporal coherence. During the least square estimation, we expect that the error is not greater than the observations. After the linear deformation extraction, we use the spatially low filtering and temporally low filtering to extract the nonlinear deformation. The spatially low filtering and temporally high filtering are used to extract atmospheric residues. Then, we remove the two parts and leave the other components as noise. If we assume that the elevation error is 0, the temporal baseline is 28 days, and then we obtained the deformation gradient along arcs for the SBAS; we calculated the arc length

of the results and found that the average value was 209.03 m. Therefore, the minimum detectable deformation gradient along arcs for the SBAS was calculated and shown in Figure 3. The minimum detectable deformation gradient of DInSAR decreases linearly with the increase in temporal coherence. A similar phenomenon was observed in the SBAS. However, within the coherence range of 0.05 to 0.6, the SBAS achieves a lower minimum detectable deformation gradient than DInSAR. This indicates that the SBAS is superior for regions with low coherence, which are primarily natural areas. Thus, the SBAS is useful for detecting geohazards. When coherence falls below 0.05 or exceeds 0.6, the minimum detectable deformation gradient of DInSAR is lower than that of SBAS. Thus, DInSAR is preferable when coherence is high enough. This is the case for LT-1. Therefore, in areas where the terrain types are simple and the vegetation is sparse enough, this advantage makes DInSAR more suitable than the SBAS.

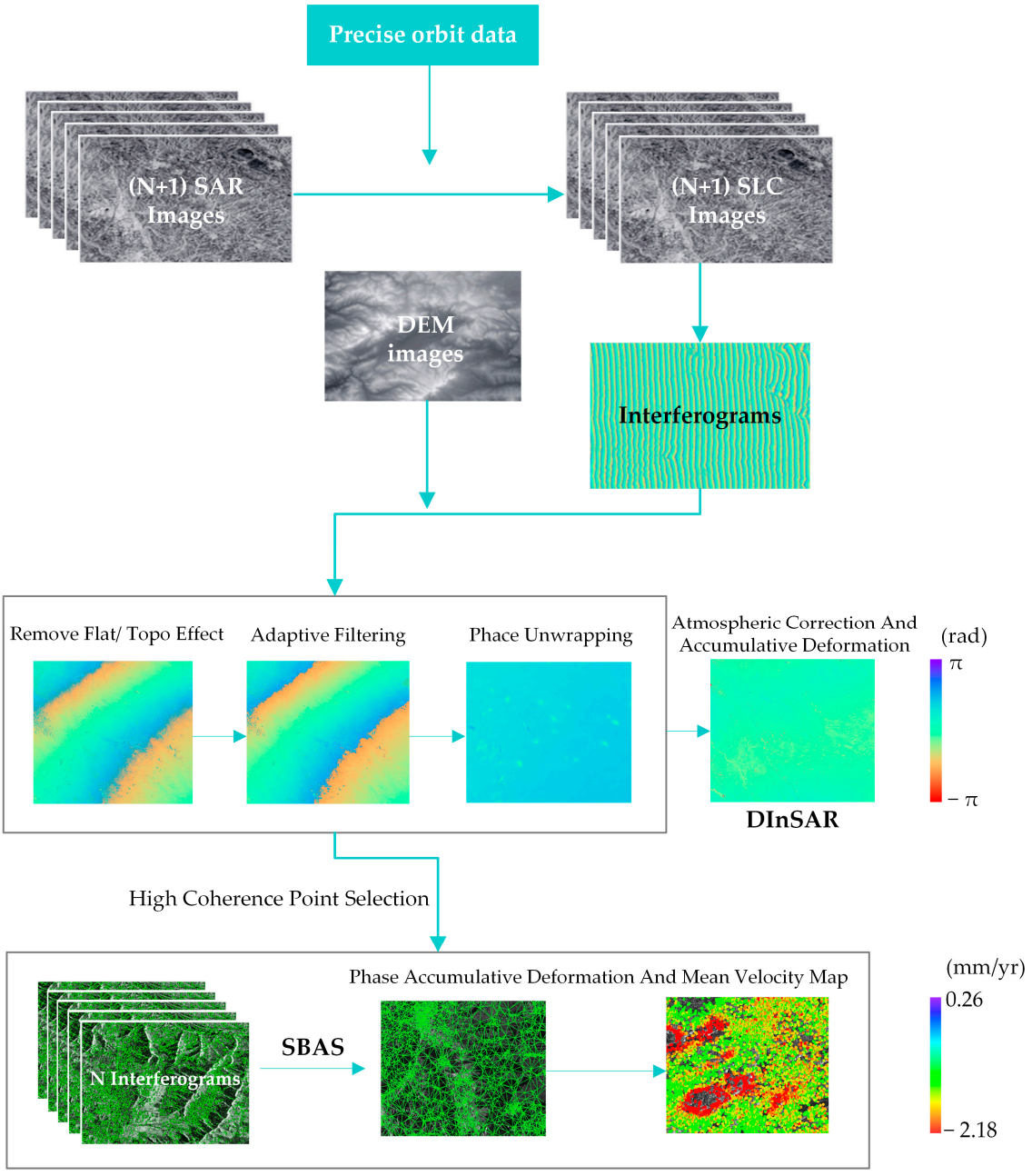


Figure 2. DInSAR and SBAS processing chains.

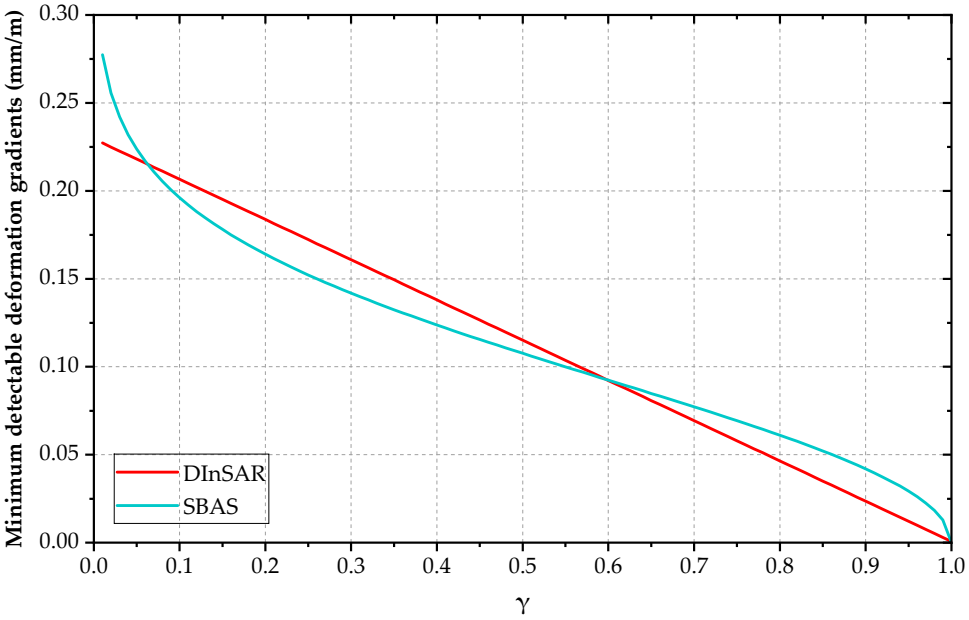


Figure 3. Relationship between deformation gradient and temporal coherence of both methods.

3. Results

We combined DInSAR and the SBAS to identify 1620 potential geohazards in Henan Province, including 1470 detected by both methods and 150 exclusively by the SBAS (Figures 4 and 5). The 150 hazards comprise 141 land-deformation sites and 9 slow-developing landslide risks. Geohazards identified by both techniques are marked with filled circles, color-coded by type with the following color scheme: purple for ground collapse, green for land deformation, gray for rockfall, orange for mud-rock flow, and bright red for landslide. Triangles represent geohazards detected only by the SBAS method.

The results revealed distinct spatial patterns of geohazards across the province. Firstly, 1340 geohazards are located in western and southern Henan and are predominantly landslides. Secondly, 139 cases are ground collapses due to underground mining, mainly in the coal-rich central and eastern regions. Thirdly, 141 land-deformation sites occur chiefly in the grain-growing areas of central and northern Henan. Provincial deformation results reveal significant surface displacement signals in western Henan, correlating with heightened geohazards [20].

The three circled points of Figure 5 highlight significant deformation. Point a marks the province's most severe deformation, measuring −296 mm. In contrast, Point b shows the greatest uplift across the region at 212 mm. Point c represents the most substantial settlement in Lingbao City (−87 mm). The SBAS results provide further insight into the deformation trends at these points, revealing high annual deformation velocities: −1470 mm/yr at point a, +499 mm/yr at point b, and −273 mm/yr at point c. These velocities indicate persistent and ongoing deformation or uplift processes.

Figure 6, Figure 7, and Figure 8 present the DInSAR and SBAS analysis results for areas a, b, and c, respectively. Each figure comprises four components: (a) DInSAR interferograms, (b) deformation velocity rate map generated by the SBAS, (c) optical image, and (d) cumulative deformation line chart. Area a, situated within an active coal mining area [13], displays continuous and extensive ground deformation resulting from long-term mining operations. Analysis of the deformation time-series reveals distinct temporal patterns, see the line chart. Deformation rates were low with small magnitudes during August–November 2023 and April–October 2024, suggesting reduced or halted mining activity. In contrast, significantly accelerated deformation occurred from November 2023 to

April 2024, attributable to seasonal deformation driven by coal-fired winter heating. Deformation resumed from October to December 2024, which is consistent with renewed mining operations. Area b, situated at a tailing dam, exhibits the most prominent uplift signal in the region. This persistent uplift is attributed to the continuous accumulation of mine waste material, primarily occurring during August 2023–May 2024 and August–October 2024. Conversely, localized settlement features observed from May to August 2024 and October–December 2024 are likely caused by the periodic cleaning of the tailing reservoir. Area c, identified as a potential landslide hazard in Lingbao City, shows significant deformation. This deformation is likely associated with rainfall events, see Figure 8. It can be inferred that heavy rainfall during August–September 2023 triggered persistent ground deformation, whereas the pronounced rainfall surge at the end of July 2024 induced a marked acceleration in the deformation rate [14].

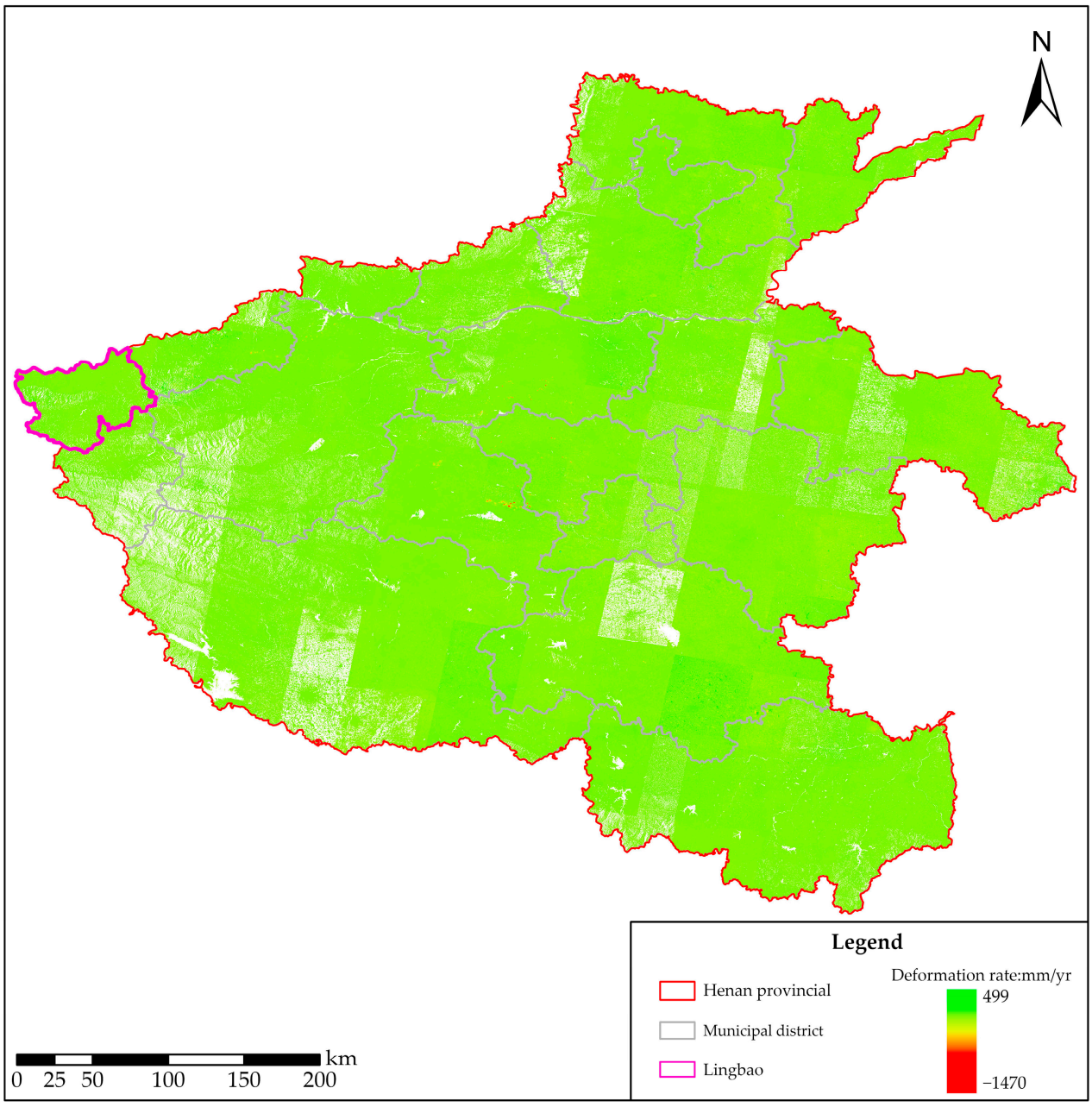


Figure 4. Deformation results of the SBAS method.

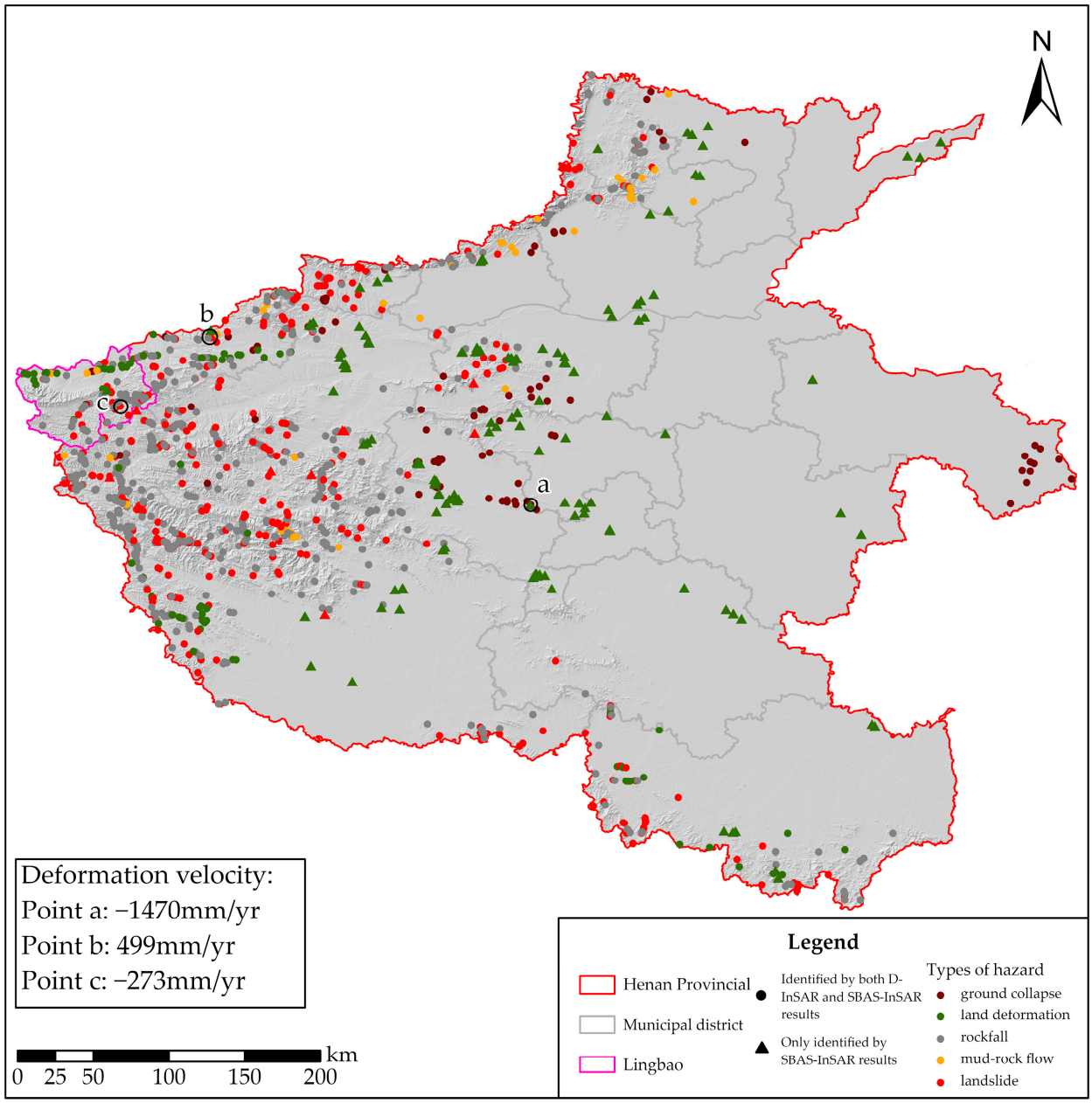


Figure 5. Types and distribution of hazards of both methods using descending-orbit data.

Figure 9 depicts land deformation areas identified only by the SBAS results. In the plain area, integration of mining-rights boundaries, optical imagery, and field surveys indicates that observed deformation stems from human activity: active open-pit operations and residual subsidence from former mining. Where the deformation lies outside mining-rights limits and field observations exclude landslides or collapse, groundwater extraction is identified as the responsible process, a conclusion supported primarily by the field survey. Areas a, b, c, and d resulted from mining-related human activities at the open-pit mine, including tailing ponds, waste dumps, and activities in non-mining operational zones. Area e exhibits residual deformation from historical underground mining activities [21]. Areas f, g, h, i, j, k, and l are primarily caused by groundwater extraction [22] for agricultural irrigation, domestic use, or industrial purposes. Furthermore, distinct deformation features were successfully interpreted by both DInSAR and SBAS in two areas: the active mining face around area a (open-pit mine), and the second area around area e, where deformation is induced by ongoing underground mining operations.

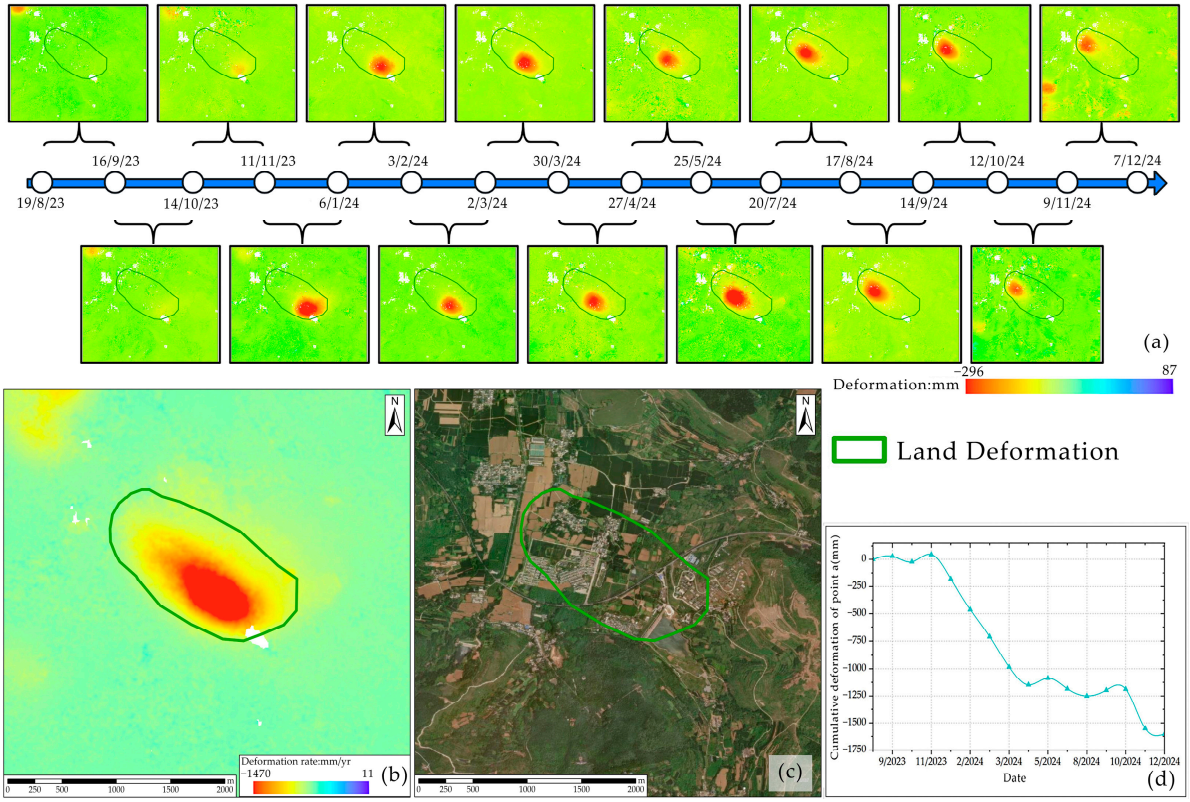


Figure 6. DInSAR and SBAS results of area a. (**a**) DInSAR results; (**b**) SBAS results; (**c**) optical image; (**d**) cumulative deformation line chart.

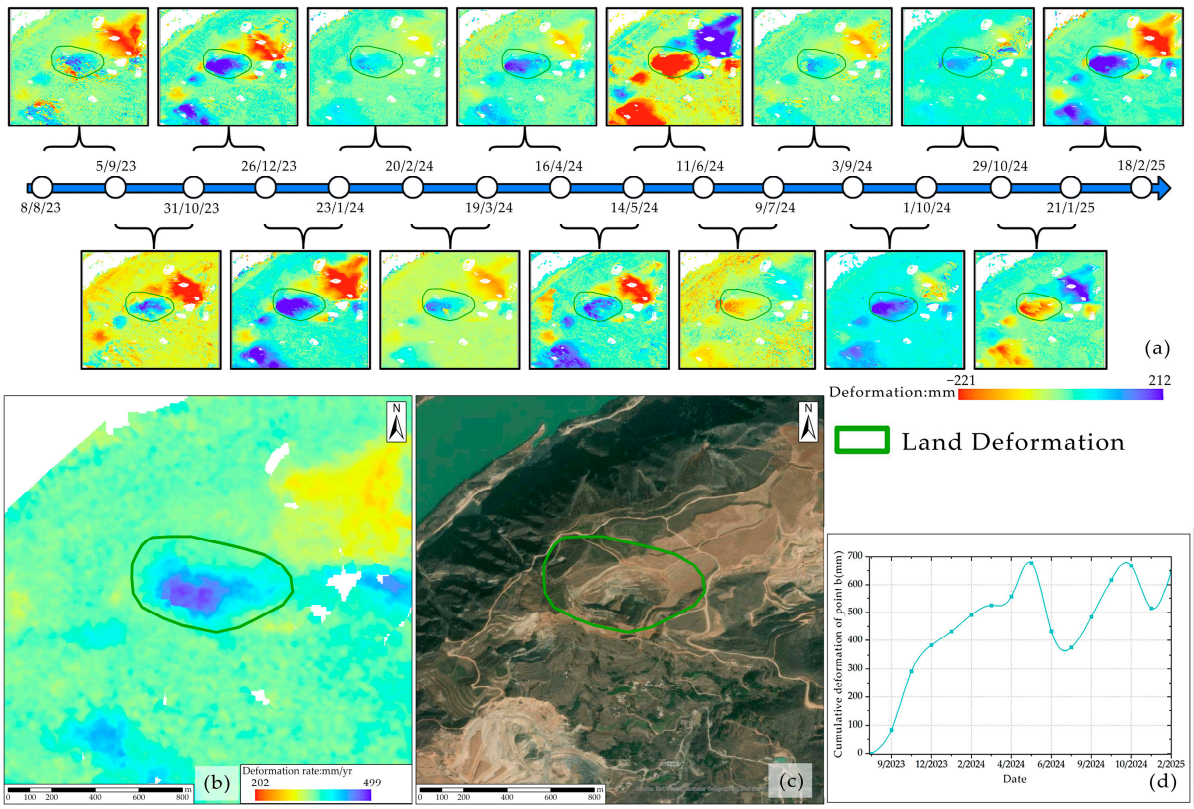


Figure 7. DInSAR and SBAS results of area b. (**a**) DInSAR results; (**b**) SBAS results; (**c**) optical image; (**d**) cumulative deformation line chart.

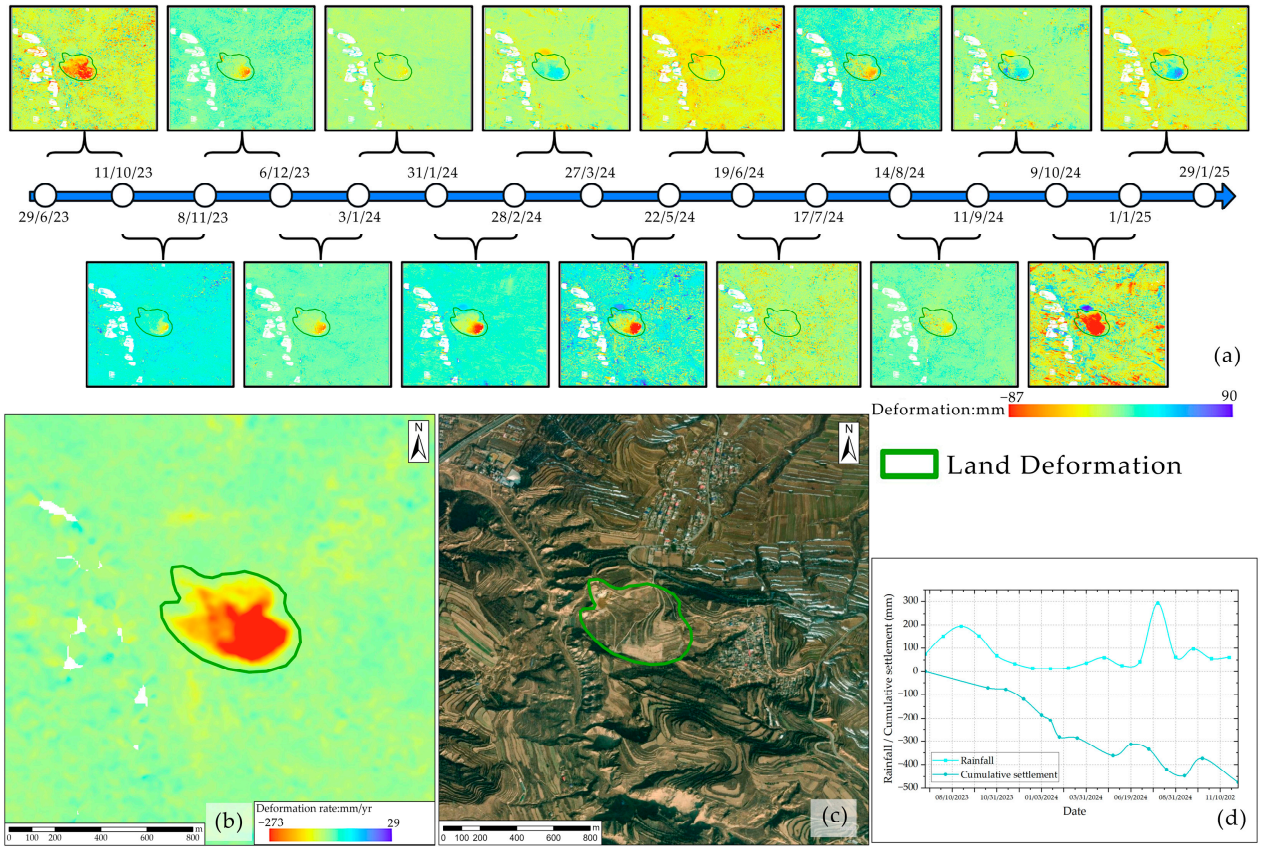


Figure 8. DInSAR and SBAS results of area c. (**a**) DInSAR results; (**b**) SBAS results; (**c**) optical image; (**d**) cumulative deformation line chart.

Figure 10 shows the nine landslide hazards only identified by the SBAS [23] results province-wide. Except for c, d, and g, the other six hazards are scattered, and the settlement amount is relatively small, which makes it difficult to identify even in the velocity results. The maximum value of deformation velocity is −157 mm/yr.

Figure 11 shows a case of land-deformation monitoring results. Part a displays DInSAR results for each time period. In contrast, b and c present the SBAS results and optical image, respectively, where the deformation field within the same green circles is significantly more pronounced. The maximum settlement measured by DInSAR is −119 mm, while the maximum settlement rate derived from the SBAS analysis is −145 mm/yr. Deformation within the green circles is difficult to discern in these results. This enhanced visibility is due to the SBAS's ability to account for accumulated deformation over time. The observed land deformation [24] at this location is consistent with the pattern shown in SBAS-only land-deformation results and is attributed to groundwater extraction for domestic and industrial use, resulting in gradual land deformation.

Figure 12 provides a case comparison of abandoned underground mining monitoring. Part a, b, and c are DInSAR results, SBAS results, and optical image, respectively. The maximum settlement measured by DInSAR is −89 mm, while the maximum settlement rate derived from the SBAS analysis is −95 mm/yr. Following mine closure, residual deformation persists over the mined-out area for an extended period. Unlike the significant, rapid collapse during active mining, this residual deformation exhibits lower deformation rates and occurs gradually over a longer timescale. Consequently, DInSAR often struggles to detect this subtle, long-term deformation. If we enlarge the temporal baseline to a year, the temporal decorrelation would be too serious to provide useful deformation information.

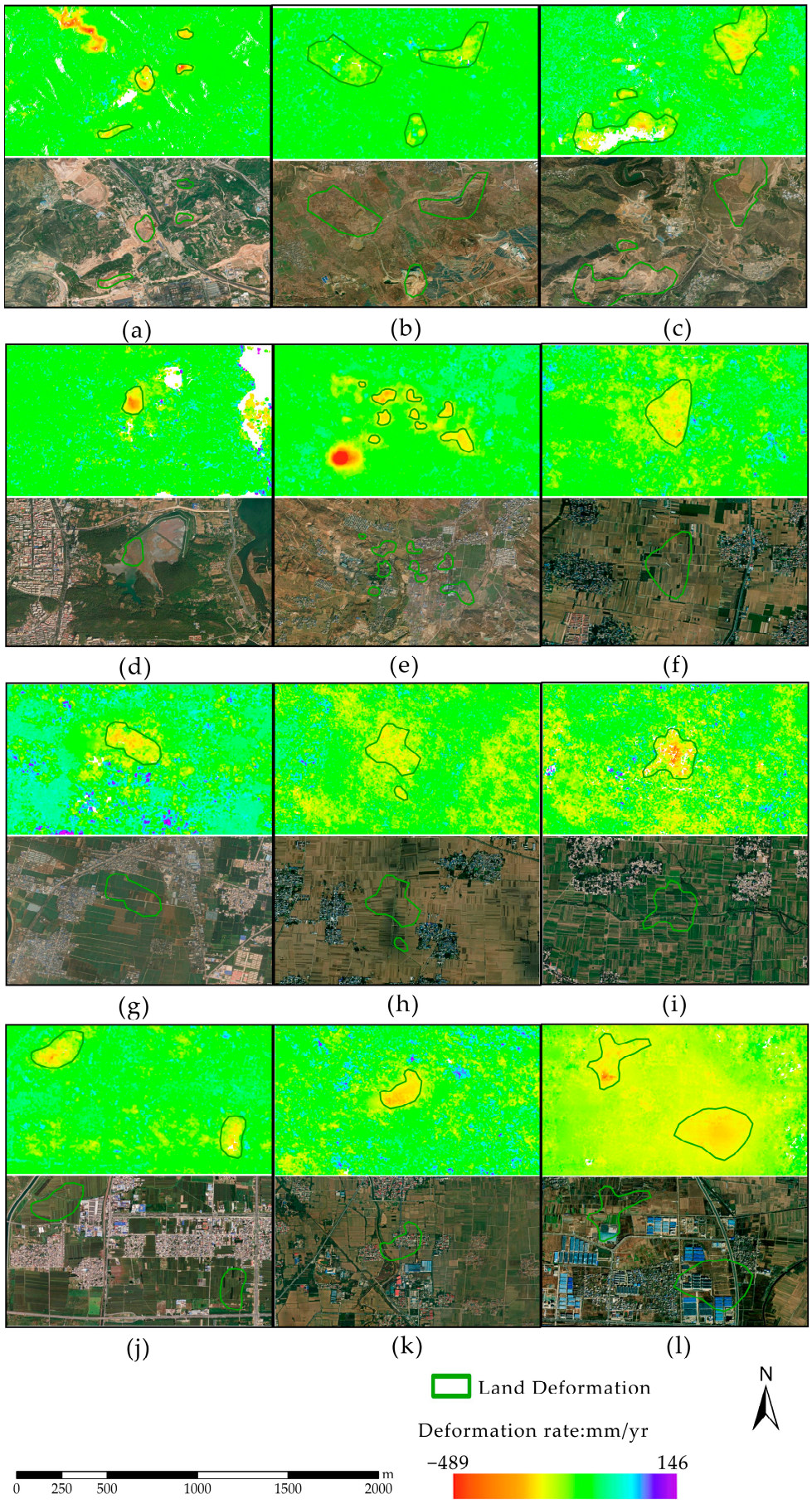


Figure 9. Deformation results of land-deformation areas only identified by SBAS. (**a**–**d**) from open-pit mining, (**e**) from historical underground mining activities, (**f**–**l**) from groundwater extraction.

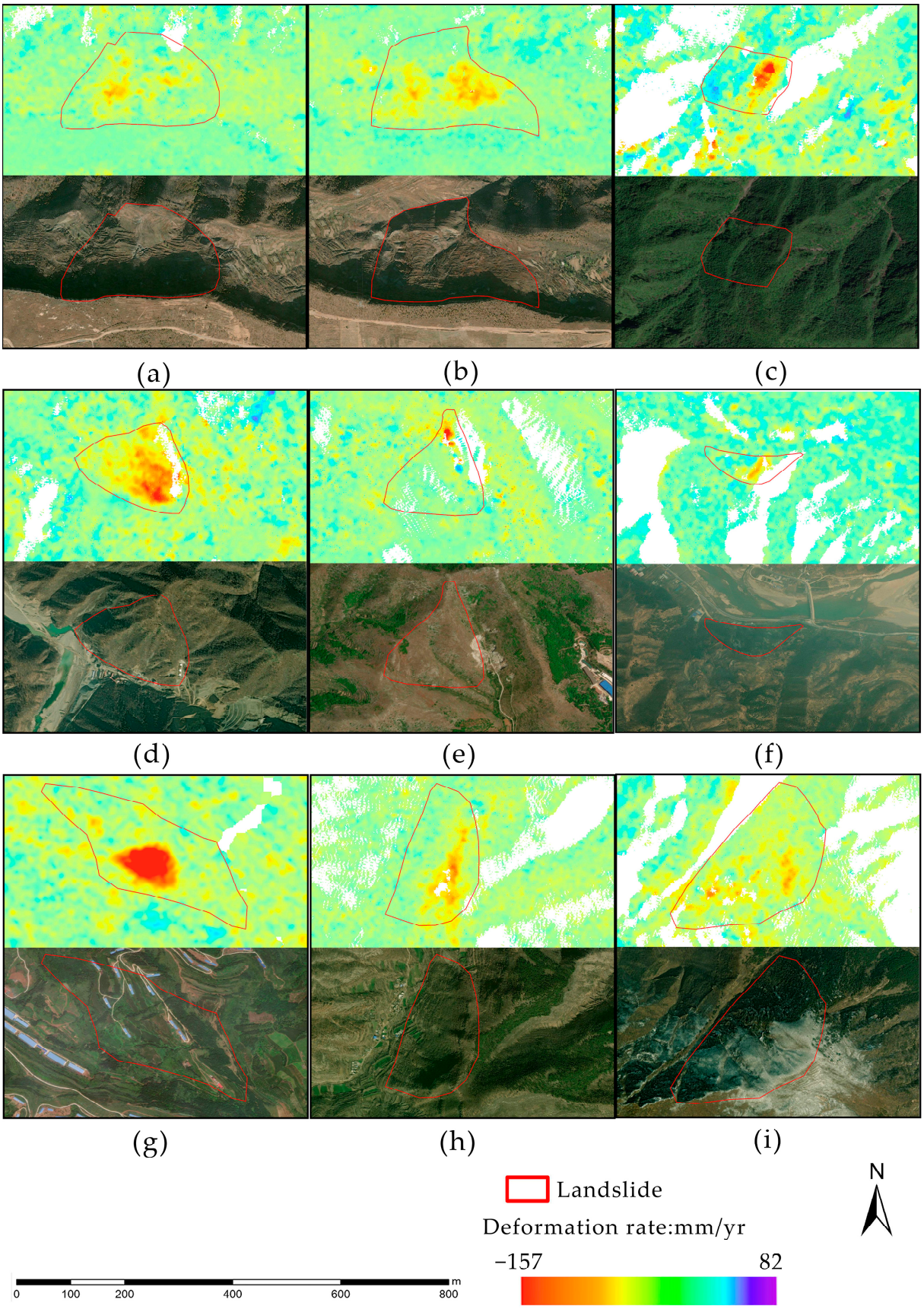


Figure 10. The nine landslide hazards identified only by SBAS results province-wide.

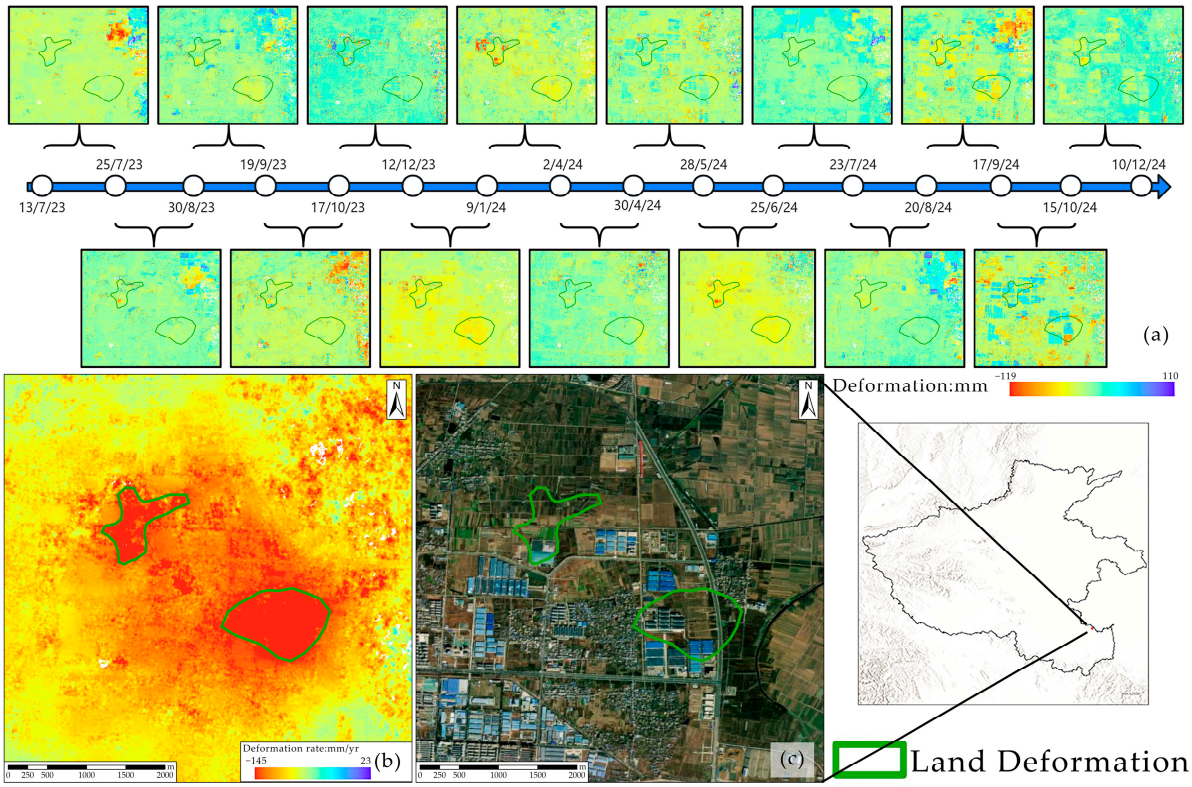


Figure 11. A case comparison between DInSAR and SBAS results of land deformation. (**a**) DInSAR results; (**b**) SBAS results; (**c**) optical image.

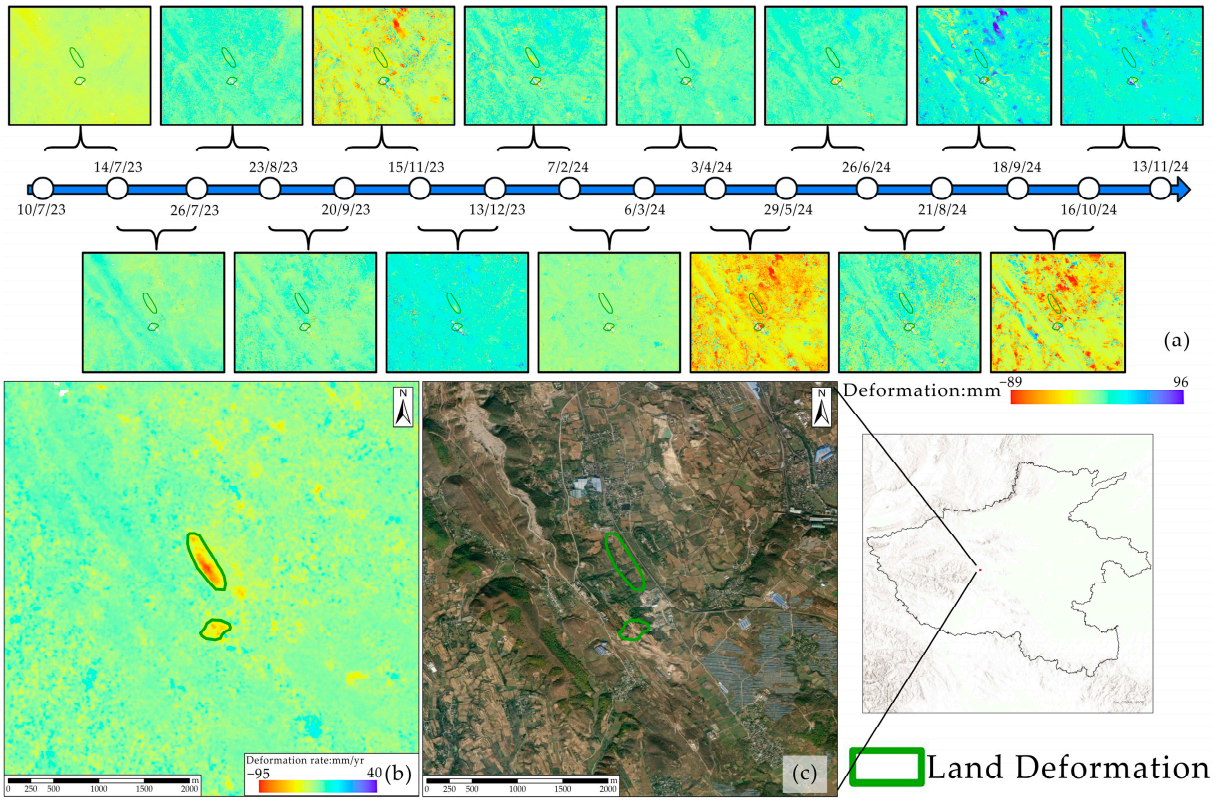


Figure 12. A case comparison between DInSAR and SBAS results for underground mining monitoring. (**a**) DInSAR results; (**b**) SBAS results; (**c**) optical image.

4. Discussion

4.1. Detailed Investigation of Typical Geohazards

Based on InSAR results, Lingbao City was selected as a key area for detailed geohazard interpretation [25] due to its diverse disaster types, high disaster density, and distinctive deformation characteristics. The terrain of Lingbao is higher in the south and lower in the north, descending in a stepwise manner with a natural gradient of 34.4%. Six landform types develop sequentially from south to north: high mountain area, low mountain area, loess plateau, piedmont alluvial fan, river terrace, and riverbed floodplain [26]. The city has a warm, temperate, and continental semi-humid monsoon climate. The annual average precipitation shows significant spatial differences, reaching 988.2 mm in the southern mountainous area and only 616.4 mm in the northern river valley plain, with 80% of the precipitation concentrated from May to October [27]. There are more than 10 major rivers in the area. Geologically, it is located on the southern margin of the Central Chinese Precambrian basement, with a double-layer structure of crystalline basement and sedimentary cover. The main fault systems are near east–west, northwest, and northeast. The basic seismic intensity is Grade 7.

May 2024 survey data identified 79 geohazards in Lingbao City: 36 collapses accounting for 45.6%, 18 landslides accounting for 22.8%, 12 debris flows accounting for 15.2%, 2 ground collapses accounting for 2.5%, and 1 ground fissure accounting for 1.3% [28]. Heavy rainfall triggers over 90% of sudden collapses, landslides, and debris flows, while mining activities directly induce ground deformation and fissures [29]. Spatially, geohazards are distributed in a belt along river valleys, such as the Zongyang River and Hongnong River [26], with a high density in areas of intense human activity, such as Zongyang Town mining area [30] and Wumu Township's cultivated slopes. A total of 70% of geohazards are located at 300–1000 m elevations. Temporally, 90% of hazards happened in July–September during peak rainfall, exhibiting a delayed effect under sustained precipitation. Disaster mechanisms demonstrate geohazards characterized by suddenness, with a short deformation–instability duration and a crack propagation rate of over 5 mm/h that are influenced by local micro-climates. In addition, debris flows triggered by mining waste have blurred source–transport boundaries, increasing the risk of mobility-related disasters [29].

Figure 13 demonstrates the deformation velocity results for Lingbao City derived from ascending and descending LT-1 data, along with interpreted deformation hazards. A total of 51 landslide hazards (LB1-LB51) were identified through detailed investigation and field survey, 14 of which were newly discovered this time. The deformation rates ranged from −410 mm/yr to 210 mm/yr.

Figure 14 presents the interpretation results of Slope LB1. Part a, b, c, d, and e are the SBAS results, GF-2 imagery, UAV oblique photography, LiDAR, and cumulative deformation map, respectively. LB1 is a newly identified hazard located in Zhouyu Village, Lingbao City, with a maximum deformation rate of −105 mm/yr. Based on the SBAS results, three points (P1, P2, and P3) were selected from the deformation center to the periphery to plot the cumulative deformation line chart. It is evident that the hazard exhibits significant deformation from June to October each year, primarily influenced by the heavy rainfall during the flood season. The approximate range of the landslide was delineated by superimposing a GF-2 optical satellite image. A 3D model of the hazard was constructed using UAV oblique photography, which facilitated the detailed interpretation of ground objects. Additionally, a digital elevation model was created with UAV LiDAR data, allowing for the interpretation of landslide characteristics such as cracks, gullies, and slopes.

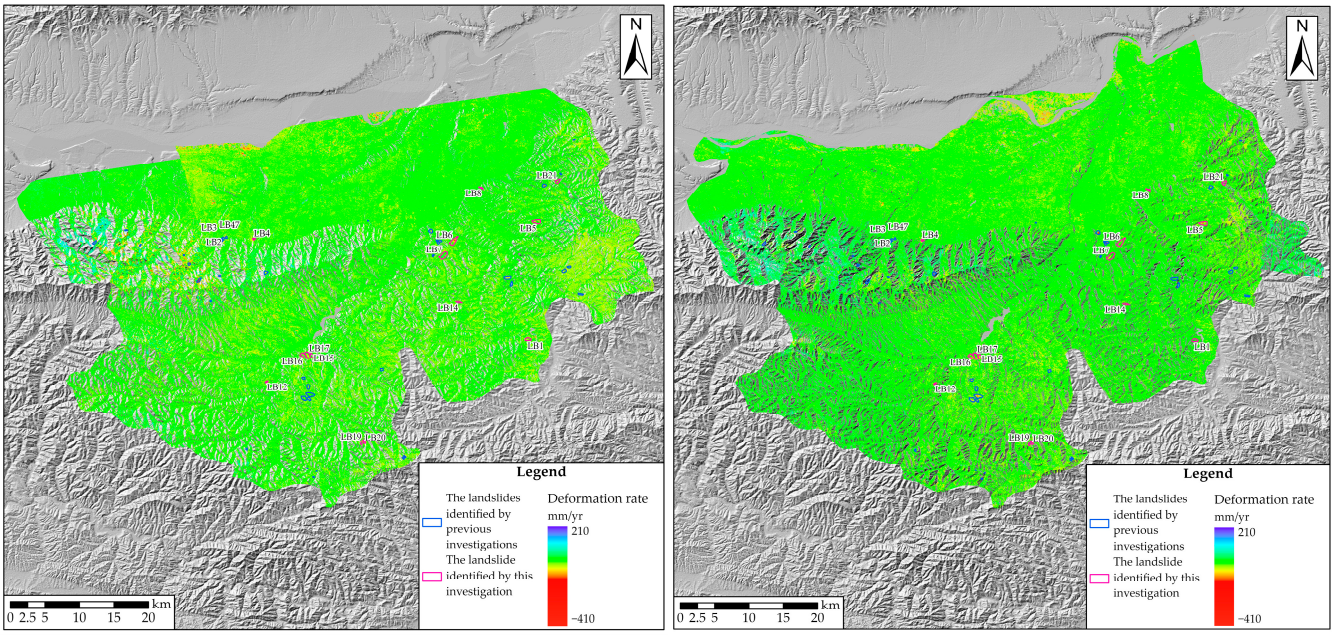


Figure 13. SBAS results for Lingbao city using ascending and descending LT-1 data. (**a**) ascending results; (**b**) descending results. The purple circle marks the newly discovered hazards by this investigation.

As is shown in Figure 15, LB2, LB3, and LB47 are three registered landslides that fall within the mining concession of a mining company, with a maximum deformation rate of −187 mm/yr. Part a, b, c, d, and e are the SBAS, GF-2 imagery, UAV oblique photography, LiDAR, and cumulative deformation, respectively. In this investigation, signs of deformation were identified at these sites. Three points (LB2-P1, LB3-P2, and LB47-P3) were selected for each landslide hazard to plot the cumulative deformation line chart. The line charts show that the deformation at these points generally follows a linear pattern, indicating that the landslides are probably influenced by human mining activities and less affected by rainfall. The extent of the landslides was delineated using GF-2 satellite imagery. UAV oblique photography was employed to construct 3D models for identifying ground objects, while UAV LiDAR data were used to create digital elevation models, which facilitated the interpretation of features such as cracks, gullies, and small slope units.

Five newly-identified landslide hazards in Lingbao were active from March 2024 to February 2025, according to ascending-orbit data, see Figure 16. Part a–b, c–d, e–f, g–h, and i–j are the SBAS results and GF-2 imagery of each hazard, respectively. k is the cumulative deformation chart of the five hazards. Analysis of the cumulative deformation line charts for each point indicates that the deformation is predominantly linear. LB6, LB12, and LB17 are terraced fields, which were easily ignored in previous investigations. LB19 and LB21 are high-elevation hazards, which were not easy to reach for investigators in the past [31].

The descending-orbit images acquired over Lingbao City acquired from June 2023 to February 2025 enabled the identification of eight previously undetected hazards, including LB4, LB5, LB7, LB8, LB14, LB15, LB16, and LB20 (Figure 17). Part a–b, c–d, e–f, g–h, i–j, k–l, and m–n are the SBAS results and GF-2 imagery of each hazard, respectively. Part o is the cumulative deformation chart of the eight hazards. Analysis of the cumulative deformation line chart for each point indicates that the deformation is predominantly linear. Utilizing optical imagery and UAV technology, it was revealed that the surfaces of LB4, LB5, LB7, LB14, LB15, and LB16 are terraced fields, which were often overlooked in previous

investigations. Meanwhile, LB8 and LB20 are classified as high-elevation hazards that were previously difficult for investigators to access.

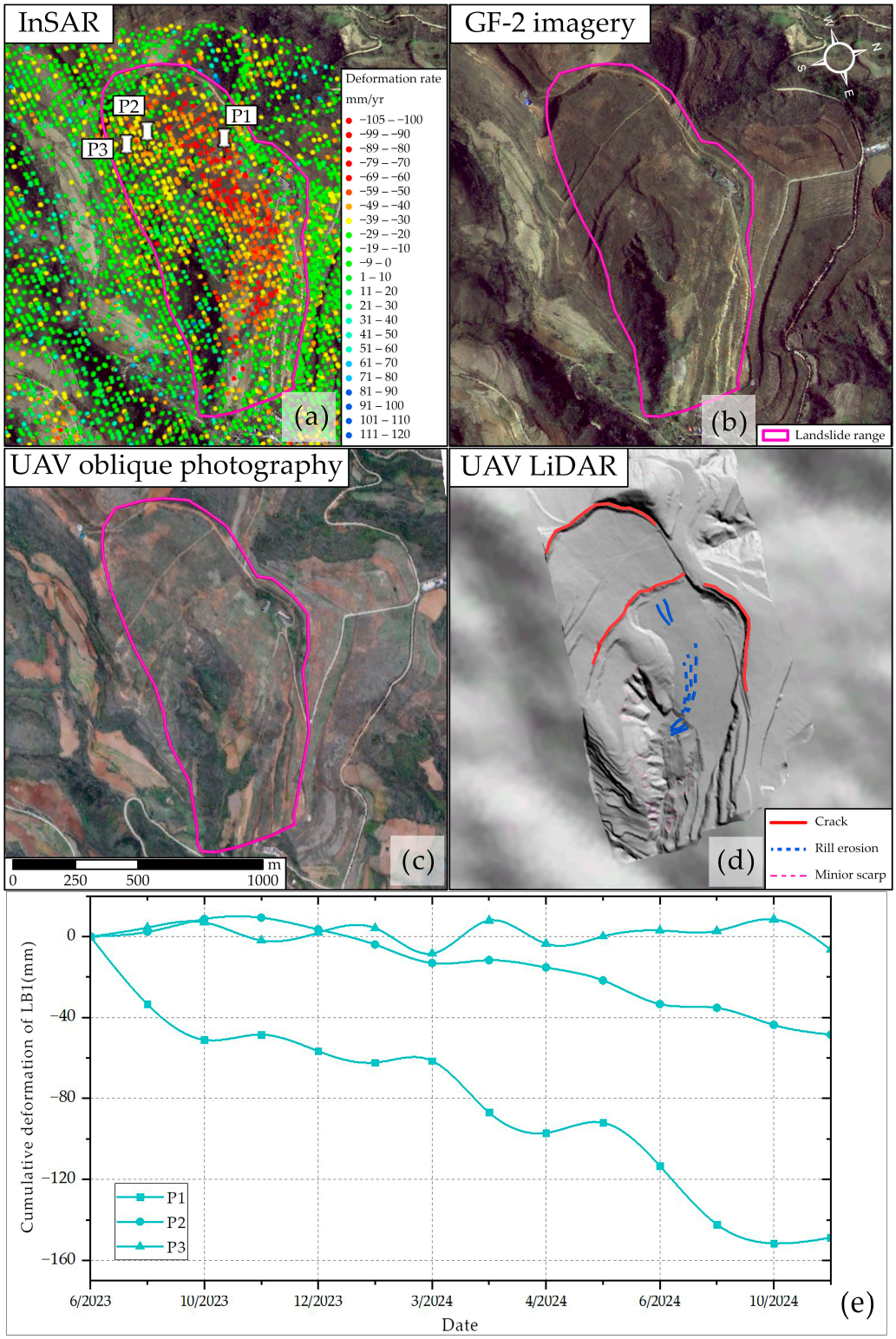


Figure 14. Interpretation results of three points in Slope LB1. (**a**) the SBAS results; (**b**) GF-2 imagery; (**c**) UAV oblique photography; (**d**) UAV LiDAR image; (**e**) cumulative deformation map. Landslide hazard outlines are delineated by red polygons in (**b**,**c**).

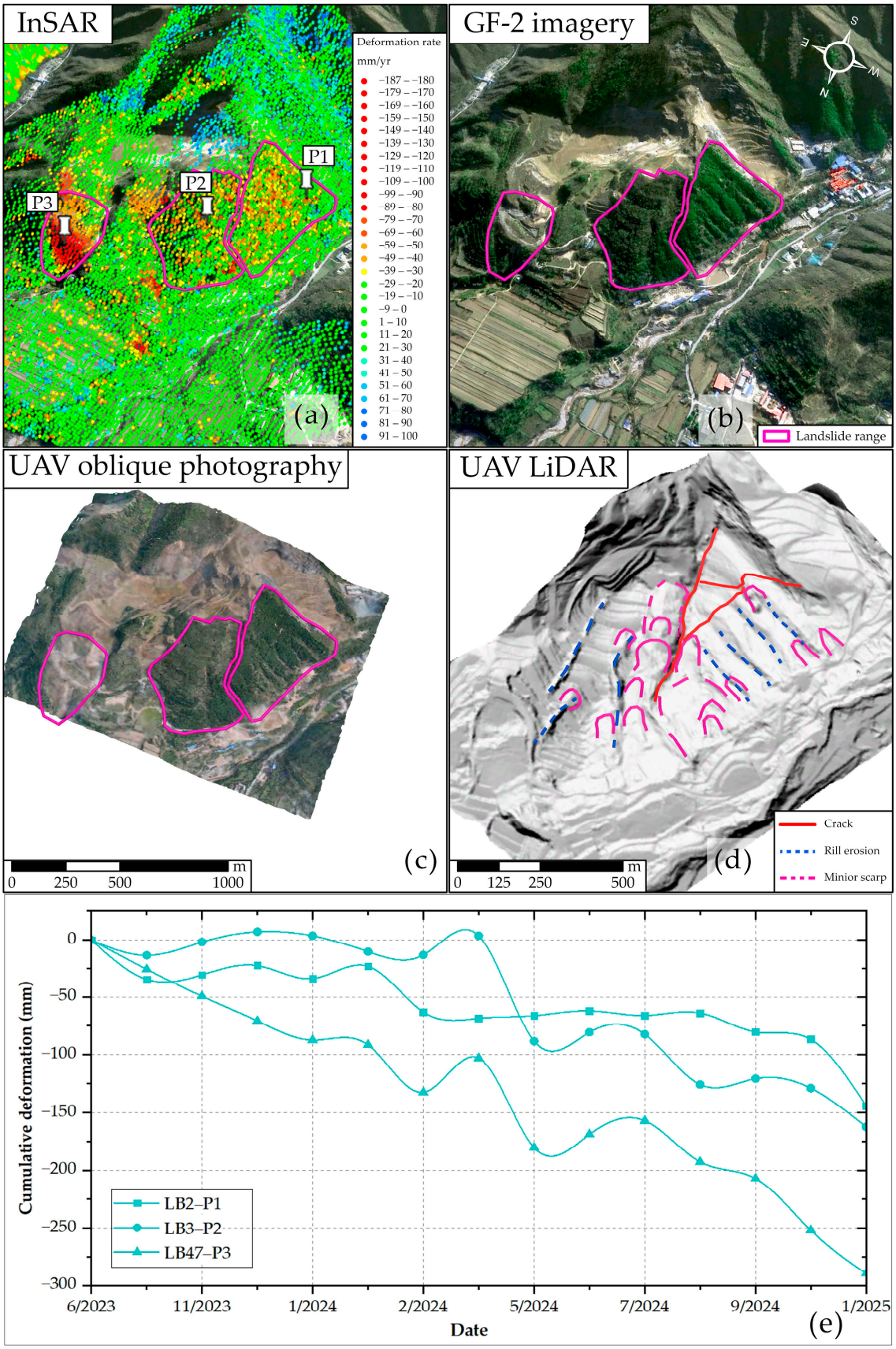


Figure 15. Interpretation results of LB2, LB3, and LB47. (**a**) SBAS results; (**b**) GF-2 imagery; (**c**) UAV oblique photography; (**d**) UAV LiDAR image; (**e**) cumulative deformation map. Landslide hazard outlines are delineated by red polygons in (**b**,**c**).

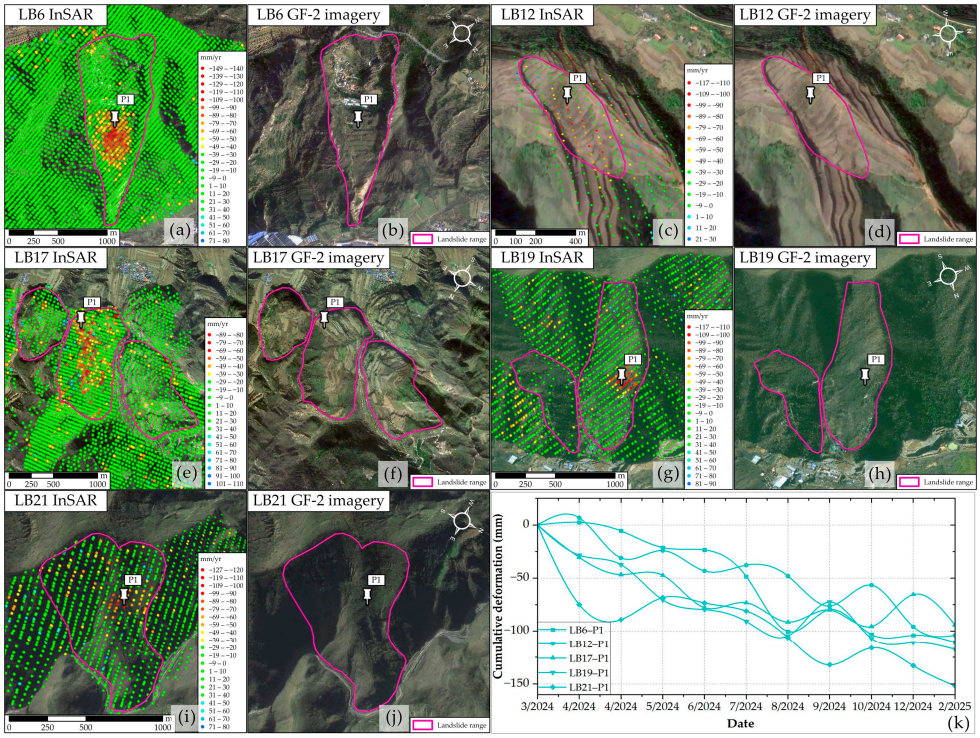


Figure 16. New landslide hazards identified in Lingbao City based on ascending-orbit data. (**a**–**j**) the SBAS results and GF-2 imagery of five hazards; (**k**) cumulative deformation charts. Landslide hazard outlines are delineated by red polygons.

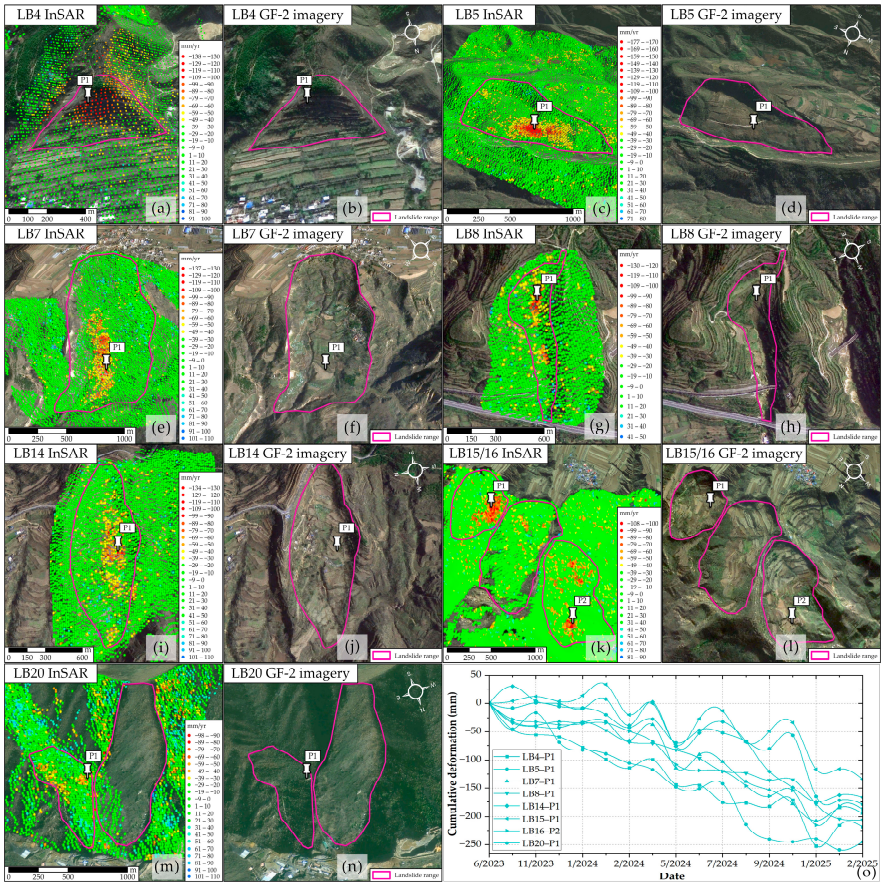


Figure 17. New landslide hazards identified in Lingbao City based on descending-orbit data. (**a**–**n**) the SBAS results and GF-2 imagery of eight hazards; (**o**) cumulative deformation charts. Landslide hazard outlines are delineated by red polygons.

4.2. The Minimum Detectable Deformation Gradients of DInSAR and SBAS

Across Henan Province, DInSAR located 1470 potential geohazards, whereas the SBAS uncovered all 1620 sites, which is 150 more than DInSAR on its own. Focusing on these 150 extra hazards, we analyzed the minimum detectable deformation gradients of both methods, see Figure 18.

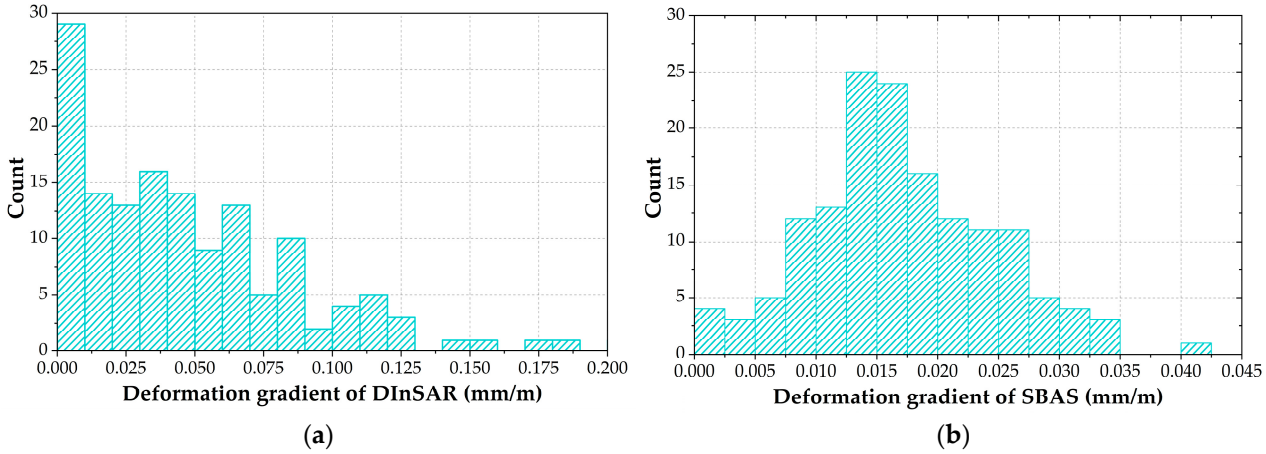


Figure 18. Deformation gradients and average coherence of DInSAR and SBAS results. (**a**,**b**) are the deformation gradients calculated from DInSAR and SBAS results, respectively.

Statistical analysis revealed that the measured minimum deformation gradient of DInSAR is 0.061 mm/m. The SBAS lowers this value to 0.017 mm/m, thanks to its mean coherence of 0.945 compared with DInSAR's 0.5. This enhanced the SBAS coherence results from effective noise suppression through short baseline interferogram combinations and multi-temporal averaging, facilitating the identification of stable targets over long time series and the successful extraction of cumulative deformation.

The smaller minimum detectable deformation gradient achieved by the SBAS demonstrates its superior capacity to reveal subtle displacement signals that are commonly masked in DInSAR by temporal decorrelation and atmospheric phase noise. Because these slow-moving hazards accumulate only limited displacement within short time spans, their signals fall below the DInSAR detection threshold. This comparison quantifies the fundamental advantage of the SBAS: multi-temporal processing enhances coherence, reduces the detectable gradient, and thereby makes the SBAS indispensable for monitoring long-term, millimeter-scale deformation.

5. Conclusions

This study used the basic deformation products derived from LT-1 data, employing both DInSAR and SBAS techniques to conduct a comprehensive geohazard survey across Henan Province. Landslides, predominantly located in western and southern Henan, constitute the largest proportion of identified hazards. Ground collapse, mainly occurring in the coal-rich central and eastern regions, represents the secondary type. Ground deformation, mostly found in the grain-growing areas of central and northern Henan, accounts for the tertiary share. Analysis identified a total of 1620 potential geohazards. Cross-validation showed that 1470 hazards were detected by both techniques, while the SBAS uniquely identified 150 hazards. Detailed investigation and field validation in Lingbao City identified 51 landslide hazards with the maximum deformation of −410 mm/yr, of which 14 hazards were newly discovered. Regarding the newly discovered geohazards in this study, their evolution will be continuously monitored.

Statistical analysis of 150 slow-moving geohazards exclusively detected by the SBAS confirms that DInSAR fails to identify these features because their average deformation gradient (0.061 mm/m) falls below DInSAR's detection threshold. Therefore, the applicability of the SBAS and DInSAR is obvious during our analysis. First of all, DInSAR outperforms the SBAS when the coherence is higher than 0.6. Secondly, the SBAS outperforms DInSAR when the coherence is between 0.05 and 0.6. Thirdly, when the coherence is lower than 0.05, DInSAR seems better, but they both lose their reliability. During the usage of the two kinds of deformation products, we actually found that DInSAR works better than the SBAS in the highly coherent regions due to its simpler data-processing flow. We always choose DInSAR to balance the data-processing cost and the success rates of geohazard identification. For the geohazards detailed in this investigation, the SBAS is more appropriate than DInSAR because we have to identify as many potential geohazards as possible. After detection of the geohazards by using InSAR and field work, we submit the results to the relevant department, i.e., the Institute of Natural Resources Monitoring and Comprehensive Land Improvement of Henan Province, to prevent the geohazards by establishing a monitoring and early warning system as well as slope protection. These findings establish a practical framework for InSAR method selection and provide critical data supporting sustainable development and disaster mitigation in Henan Province, with significant implications for regional geohazard monitoring.

The effectiveness of LT-1 for large-scale geohazard monitoring has been robustly demonstrated by this provincial deformation-monitoring research. At present, LT-1 data have been used as the main SAR data resources in Henan Province. In addition, the work patterns of Henan have been promoted in many other provinces, including Shaanxi, Sichuan, Guizhou, etc. Given the efficiency of the SBAS and DInSAR, we are now considering separating the two technologies into different scenarios, e.g., DInSAR for screening some quick geohazards and the SBAS for geohazard monitoring. This deepening of application and promotion will efficiently drive the application of InSAR technology in the industry.

Author Contributions: All the authors participated in editing and reviewing the manuscript. Conceptualization, J.L. and T.L.; draft manuscript, J.L.; methodology, J.L. and T.L.; statistical analysis, L.W. and L.G.; visualization, J.L. and X.Z. (Xuefei Zhang); software, T.L., X.Z. (Xuefei Zhang) and X.Z. (Xiang Zhang); review and editing, X.T. and X.Z. (Xiang Zhang); supervision, X.T. All authors have read and agreed to the published version of the manuscript.

Funding: This work was supported by National Key R&D Program of China (2023YFB3904905).

Data Availability Statement: The data presented in this study are available on request from the corresponding author due to privacy reasons.

Acknowledgments: The authors thank to the Henan Institute of Remote Sensing, China, for its invaluable support during the experiment.

Conflicts of Interest: The authors declare no conflicts of interest.

References

1. Henan Provincial Department of Land and Resources. The 13th Five-Year Plan for Geological Disaster Prevention and Control in Henan Province. Available online: http://hn.cnr.cn/tbgz/20170719/t20170719_523857086.shtml (accessed on 4 September 2025).
2. Zhang, Y.; Ci, H.; Yang, H.; Wang, R.; Yan, Z. Rainfall-Induced Geological Hazand Susceptibility Assessmentin the Henan Section ofthe Yellow River Basin: Multi-Model Approaches Supporting Disaster Mitigation and Sustainable Development. *Sustainability* **2025**, *17*, 4348. [CrossRef]
3. Tang, X.; Li, T.; Chen, J.; Wei, C.; Zhang, X.; Liu, Y.; Liu, D.; Zhang, X.; Zhou, X.; Lu, J.; et al. Twin-Satellite Constellation Design and Realization for Terrain Mapping and Deformation Monitoring: LuTan-1. *IEEE Trans. Geosci. Remote Sens.* **2025**, *63*, 5214014. [CrossRef]

4. Wang, R.; Liu, K.; Liu, D.; Ou, N.; Yue, H.; Chen, Y.; Yu, W.; Liang, D.; Cai, Y. LuTan-1: An Innovative L-band Spaceborne Bistatic Interferometric Synthetic Aperture Radar Mission. *IEEE Geosci. Remote Sens. Mag.* **2024**, *13*, 58–78. [CrossRef]
5. Li, T.; Tang, X.; Li, S.; Zhou, X.; Zhang, X.; Xu, Y. Classification of foundational deformation products for L-band differential interferometric SAR satellites. *J. Surv. Mapp.* **2023**, *52*, 770–779.
6. Zhang, L.; Jia, H.; Lu, Z.; Liang, H.; Ding, X.; Li, X. Minimizing height effects in MTInSAR for deformation detection over built areas. *IEEE Trans. Geosci. Remote Sens.* **2019**, *57*, 9167–9176. [CrossRef]
7. Tomás, R.; Li, Z. Earth Observations for Geohazards: Present and Future Challenges. *Remote Sens.* **2017**, *9*, 194. [CrossRef]
8. Dong, J.; Liao, M.; Xu, Q.; Zhang, L.; Tang, M.; Gong, J. Detection and displacement characterization of landslides using multi-temporal satellite SAR interferometry: A case study of Danba County in the Dadu River Basin. *Eng. Geol.* **2018**, *240*, 95–109. [CrossRef]
9. Yang, W.; Niu, R.; Si, R.; Li, J. Geological Hazard Susceptibility Analysis and Developmental Characteristics Based on Slope Unit, Using the Xinxian County, Henan Province as an Example. *Sensors* **2024**, *24*, 2457. [CrossRef]
10. Henan Provincial Department of Natural Resources. Henan Provincial Natural Resources Statistical Bulletin. Available online: https://dnr.henan.gov.cn/ (accessed on 4 September 2025).
11. Zhou, B.; Xie, H.; Wen, G. The susceptibility zoning of rainfall-type geological hazards in Henan Province based on erosion cycle theory. *J. North China Univ. Water Resour. Electr. Power (Nat. Sci. Ed.)* **2024**, *45*, 92–101. [CrossRef]
12. Casu, F.; Manzo, M.; Lanari, R. A quantitative assessment of the SBAS algorithm performance for surface deformation retrieval from DInSAR data. *Remote Sens. Environ.* **2006**, *102*, 195–210. [CrossRef]
13. LandSAR. Available online: http://sasclouds.com/chinese/about/software/LandSAR (accessed on 30 August 2025).
14. Gaber, A.; Darwish, N.; Koch, M. Minimizing the Residual Topography Effect on Interferograms to Improve DInSAR Results: Estimating Land Subsidence in Port-Said City, Egypt. *Remote Sens.* **2017**, *9*, 752. [CrossRef]
15. Generic Atmospheric Correction Online Service for InSAR (GACOS). Available online: http://www.gacos.net/ (accessed on 5 September 2025).
16. Baran, I.; Stewart, M.; Claessens, S. A new functional model for determining minimum and maximum detectable deformation gradient resolved by satellite radar interferometry. *IEEE Trans. Geosci. Remote Sens.* **2005**, *43*, 675–682. [CrossRef]
17. Jiang, M.; Li, Z.W.; Ding, X.L.; Zhu, J.J.; Feng, G.C. Modeling minimum and maximum detectable deformation gradients of interferometric SAR measurements. *Int. J. Appl. Earth Obs. Geoinf.* **2011**, *13*, 766–777. [CrossRef]
18. Ferretti, A.; Prati, C.; Rocca, F. Permanent scatterers in SAR interferometry. *IEEE Trans. Geosci. Remote Sens.* **2001**, *39*, 8–20. [CrossRef]
19. Li, T. Deformation Monitoring by Multi-Temporal InSAR with Both Point and Distributed Scatterers. Ph.D. Thesis, Southwest Jiaotong University, Chengdu, China, 2014.
20. Xu, Q. Understanding and Consideration of Related Issues in Early Identification of Potential Geohazards. *Geomat. Inf. Sci. Wuhan Univ.* **2020**, *45*, 1651–1659.
21. Ji, Y.; Zhang, X.; Li, T.; Fan, H.; Xu, Y.; Li, P.; Tian, Z. Mining Deformation Monitoring Based on Lutan-1 Monostatic and Bistatic Data. *Remote Sens.* **2023**, *15*, 5668. [CrossRef]
22. Calò, F.; Ardizzone, F.; Castaldo, R.; Lollino, P.; Tizzani, P.; Guzzetti, F.; Lanari, R.; Angeli, M.-G.; Pontoni, F.; Manunta, M. Enhanced landslide investigations through advanced DInSAR techniques: The Ivancich case study, Assisi, Italy. *Remote Sens. Environ.* **2014**, *142*, 69–82. [CrossRef]
23. Dong, J.; Zhang, L.; Tang, M.; Liao, M.; Xu, Q.; Gong, J.; Ao, M. Mapping landslide surface displacements with time series SAR interferometry by combining persistent and distributed scatterers: A case study of Jiaju landslide in Danba, China. *Remote Sens. Environ.* **2018**, *205*, 180–198. [CrossRef]
24. Li, G.; Zhao, C.; Wang, B.; Peng, M.; Bai, L. Evolution of spatiotemporal ground deformation over 30 years in Xi'an, China, with multi-sensor SAR interferometry. *J. Hydrol.* **2023**, *616*, 128764. [CrossRef]
25. Dai, K.; Shen, Y.; Wu, M.; Feng, W.; Dong, X.; Zhuo, G.; Yi, X. ldentification of potential landslides in Baihetan Dam area before theimpoundment by combining InSAR and UAV survey. *Acta Geod. Cartogr. Sin.* **2022**, *51*, 2069–2082. [CrossRef]
26. Zhang, M.; Xu, G. Study on the development characteristics and distribution law of geological hazards in Lingbao City. *Chin. J. Soil Water Conserv.* **2017**, 47–50.
27. Xing, Y.; Zhang, Y. Characteristics, distribution and prevention countermeasures of geological hazards in Lingbao City, Henan Province. *J. Henan Polytech. Univ.* **2006**, *25*, 5.
28. Lingbao Natural Resources and Planning Bureau. Lingbao Natural Resources and Planning Bureau Announces Existing Geological Disaster Hazard Points. Available online: https://www.lingbao.gov.cn/21820/616970880/1883707.html (accessed on 4 September 2025).
29. Zhenbo, N. Exploration of Mine Geological Environment Control Scheme in Xiaoqinling Mining Area of Henan Province. *World Nonferrous Met.* **2019**.

30. Hu, L.; Tomás, R.; Tang, X.; Vinielles, J.L.; Herrera, G.; Li, T.; Liu, Z. Updating Active Deformation Inventory Maps in Mining Areas by Integrating InSAR and LiDAR Datasets. *Remote Sens.* **2023**, *15*, 996. [CrossRef]
31. Xu, Q.; Dong, X.; Li, W. Early identification and monitoring and early warning of major geological hazards based on space-air-ground integration. *Geomat. Inf. Sci. Wuhan Univ.* **2019**, *44*, 7.

Disclaimer/Publisher's Note: The statements, opinions and data contained in all publications are solely those of the individual author(s) and contributor(s) and not of MDPI and/or the editor(s). MDPI and/or the editor(s) disclaim responsibility for any injury to people or property resulting from any ideas, methods, instructions or products referred to in the content.